

TRIMARAN: A Toolbox for Radiometric Imaging with Microwave ARrays of ANTennas

Eric Anterrieu^a

Centre d'Études Spatiales de la Biosphère (CESBio),
Université de Toulouse & CNRS-UMR5126, 18 avenue Edouard Belin, 31400 Toulouse, France

Keywords: Antennas Arrays, Aperture Synthesis, Radiometry, Imaging.

Abstract: This article aims at describing a Matlab toolbox named TRIMARAN intended to be used for Radiometric Imaging with Microwave ARrays of ANTennas. Of course, only a few functions, the most important ones, out of the 200 included in the toolbox are discussed and illustrated. In addition to this overview of TRIMARAN, some concrete usages made by researchers, engineers or students are shown to illustrate the capabilities of this toolbox. It has been used for designing aperture synthesis imaging radiometers and for quantifying instrument performances as well as for discovering and for learning many aspects of microwave remote sensing by aperture synthesis with realism.

1 INTRODUCTION

Aperture synthesis (Brouw, 1975) is a technique that mixes the signals kept by a collection of elementary antennas (Christiansen and Högbom, 1987) to produce images having the same angular resolution as that obtained with an instrument the size of the entire collection. It has been used successfully in radio astronomy since the 1950s (VLA, VLBI, VLBA...) (Thompson et al., 1980; Cohen, 1973; Napier et al., 1994) as well as in Earth remote sensing from space since the 1990s (ESTAR, SMOS...) (Vine et al., 1994; Barré et al., 2008; McMullan et al., 2008). Unlike total power radiometers that point accurately in many directions to measure the antenna temperature and thus compose a brightness temperature map, aperture synthesis imaging radiometers combine the signals kept by every elementary antenna, electronically or numerically, in order to produce a brightness temperature map with the aid of a computer. There are two ways to combine these elementary signals, known as multiplicative synthesis and additive synthesis. The former combines these antennas signals by pairs in a cross-correlator to perform synthetic aperture interferometry, whereas the latter mixes them all together to operate digital beam forming (Anterrieu et al., 2022).

TRIMARAN is a Matlab (The MathWorks, a)

toolbox that offers users the opportunity to play numerically with both paradigms on the simulation of the radio signals kept by each elementary antenna and on their combination to produce either complex visibilities (multiplication synthesis in interferometry) or antenna array maps (additive synthesis with beam forming). It is able to process them with up-to-date regularized inversion methods for retrieving the brightness temperature distribution of the scene under observation. For both approaches, TRIMARAN is capable of simulating data and of inverting them for an observed scene in the far-field region of the antenna array as well as in the near-field zone (Anterrieu et al., 2024), in ground based as well as in airborne or spaceborne situations. In every case TRIMARAN can also digest real data from an actual instrument. Moreover, as an open-source software subject to evolutions and to improvements, it will be able to process real data from future instruments like it does today with SMOS.

From a practical point of view, TRIMARAN is a self-sufficient collection (no additional toolbox required) of about 200 Matlab functions written in accordance with the MathWorks programming standards. They are divided into 9 thematic groups (orbitography, antenna array, antenna patterns, field of view, instrument modeling, radio signals, brightness temperature maps, graphic and others) that are briefly presented with illustrations in section 2. TRIMARAN relies on multidisciplinary knowledge (microwave ra-

^a  <https://orcid.org/0009-0007-2233-9098>

diometry, antenna theory, applied mathematics, signal & image processing). It is intended for, and it is used by, students at master science level for discovering playfully and for learning rigorously many aspects of microwave remote sensing by aperture synthesis with realism. It is also meant for, and used by, engineers from space industry and agencies for quickly designing aperture synthesis imaging radiometers and for practically quantifying instrument performances. It has been operated recently by researchers for simulating a huge dataset to implement and to evaluate the performances of a deep learning approach for the inversion of the complex visibilities provided by the imaging radiometer MIRAS onboard the SMOS mission of the European Space Agency (ESA). Some of these concrete usages are shown in section 3 to illustrate the capabilities of TRIMARAN.

2 FUNCTIONS OVERVIEW

As outlined in the introduction, TRIMARAN is a collection of about 200 Matlab functions (for ease of reading, all elements of the Matlab language are written here in blue with a fixed font). Of course, only few of these functions are discussed or illustrated in this section. For the others, the user is invited to discover them with the `lookfor` facility and with the in-line examples accessible from the `help` command. Indeed, all the functions of TRIMARAN meet MathWorks programming standards and for most of them an additional section of the in-line help entitled “Example” has been added in order to provide the user with illustrating usages of the function, while waiting for a user guide to be written!

2.1 Orbitography

The function `CircularOrbit` returns the orbital period T and the orbital velocity v for a circular orbit at a given elevation h around the Earth. If h lies in an appropriate range, it also returns the required inclination i for a sun-synchronous orbit, otherwise 90° is returned and the orbit is a polar one. For the SMOS mission, these elements are:

```
> h=771E+03;
> [i,T,v]=CircularOrbit(h)
i = 98.4526
T = 6.0068e+03
v = 7.4707e+03
```

Although this modeling is very basic, it is sufficient to conduct pre-studies and if necessary it can be replaced by a finer model. As a comparison between

this circular orbit approximation and the most up-to-date orbital mechanics codes used by CNES and ESA (Barré et al., 2008), with an average elevation of 771 Km the official orbital period of SMOS is given for 6004.5 s and its inclination for 98.445° , whereas they are estimated here around 6006.8 s and 98.453° , respectively.

The function `CircularOrbitPropagate` is a forward-backward orbit propagator that returns the geographic coordinates (Chang, 2016) at given dates t starting from a given location at $t = 0$. It also returns the direction of the passes (ascending or descending). Hereafter are the few lines to calculate two circular orbits passing over London:

```
> LatS=dms2deg(51,30,26);
> LonS=dms2deg(0,7,39);
> [Lon,Lat,pass]= ...
    CircularOrbitPropagate(h,i,'Asc', ...
        LonS,LatS,linspace(-T,T,1000));
> Asc=strfind(pass,'A');
> Dsc=strfind(pass,'D');
> figure;plot(Lon(Asc),Lat(Asc),'r.', ...
    Lon(Dsc),Lat(Dsc),'g. ');
> geoplotWORLD;
> legend('Asc','Dsc');
```

The geographic coordinates returned in `Lat` and `Lon` are plotted on Figure 1 together with the world's coastlines drawn with the function `geoplotWORLD`.

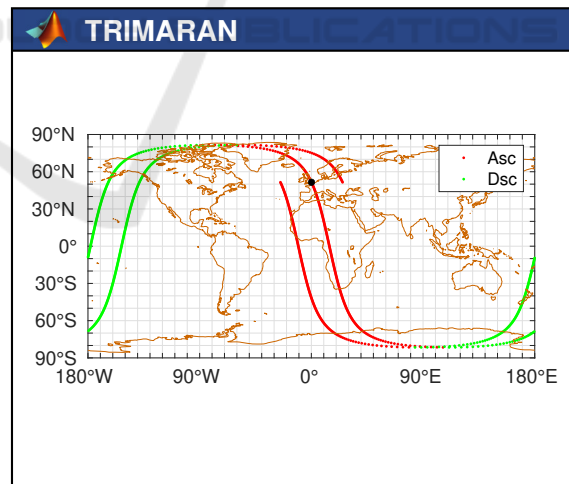


Figure 1: Example of ascending (red) and descending (green) circular orbits passing over London (black dot), as returned by the function `CircularOrbitPropagate`.

2.2 Antenna Array

The function `AntennaArray` returns the coordinates of the elementary antennas, the antennas pairs of every baseline, the components of the baselines and

the corresponding Fourier frequencies with their redundancy.... Many geometries (circle, octagon, hexagon, square, triangle, cross, Y) are available for any number of elementary antennas regularly spaced with a short spacing d and operating at a central wavelength λ_o . As the guiding thread of this presentation is the SMOS mission operating in the $B_o = 20$ MHz protected band centered on $f_o = 1413.5$ MHz, parameters of the MIRAS antenna array are available from the high-level function `SMOSarray`:

```
> Bo=20E+06;
> Fo=1413.5E+06; Lo=299792458/Fo;
> d=0.875;
> [~,~,Xa,Ya,cal,~,P,Q,~,~,Ub,Vb, ...
~,~,~,Uf,Vf,Rf]=SMOSarray(90,d,Lo);
> figure;plotAA(Xa,Ya,cal);
> figure;plotFF(Uf*Lo,Vf*Lo,Rf);
```

The antenna array of MIRAS with its 69 elementary antennas regularly spaced with $d = 0.875\lambda_o$ on the three arms of a (rotated) Y is shown on Figure 2 where the cartesian coordinates X_a and Y_a are reported. The corresponding uv-coverage is shown on Figure 3 where the Fourier frequencies U_f and V_f are plotted with a color indicating the redundancy R_f .

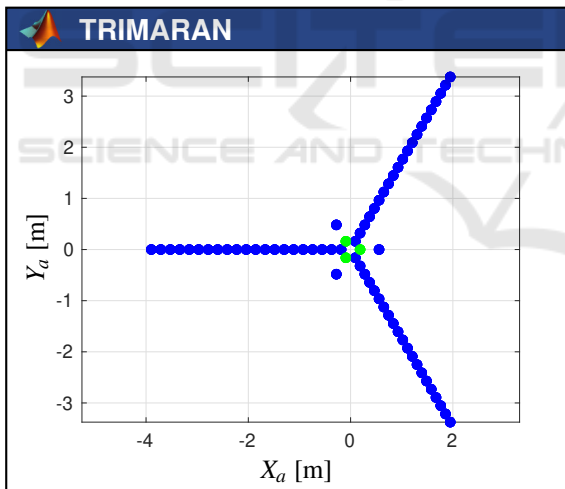


Figure 2: MIRAS, the antenna array of the SMOS space mission with 69 elementary antennas, as plotted by the function `plotAA` (those in green are used for calibration purpose). The shortest spacing is $d = 0.875\lambda_o \simeq 18.6$ cm and the longest baseline is $21\sqrt{3}d \simeq 6.75$ m.

2.3 Field of View

The paired functions `plotFOV_cart` and `plotFOV_hexa` plot the field of view at instrument level where aperture synthesis takes place. For the MIRAS instrument onboard SMOS that is tilted forwardly from the Nadir direction with an

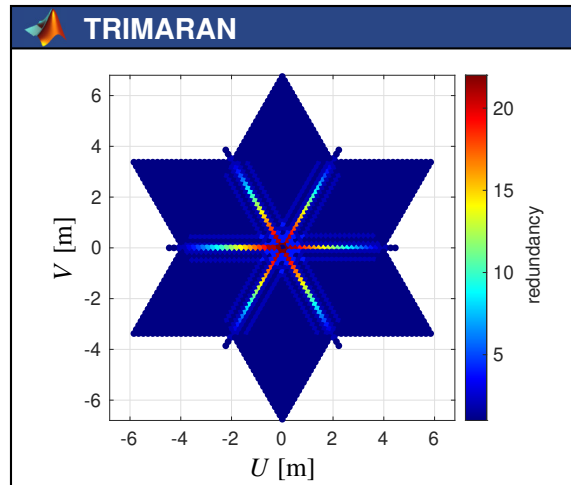


Figure 3: The uv-coverage of MIRAS with its 2791 Fourier frequencies, as plotted by the function `plotFF`. The redundancy varies from 1 to 22 (for the shortest spacing).

angle $\epsilon = 31.2^\circ$, the result is shown on Figure 4:

```
> tilt=32.5;
> figure;plotFOV_hexa(h,tilt,d,90,60.6);
```

Likewise, the twinned functions `geoplotFOV_cart` and `geoplotFOV_hexa` plot the field of view at ground level, as shown on Figure 5:

```
> figure;geoplotFOV_hexa(h,i,'Asc', ...
```

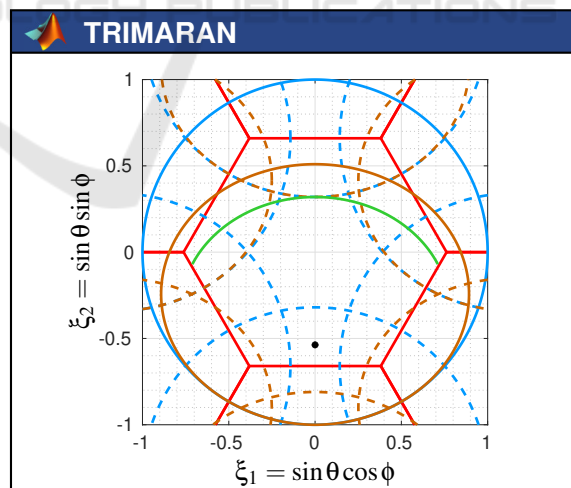


Figure 4: Hexagonal field of view of SMOS at instrument level, as plotted by the function `plotFOV_hexa`. Here the MIRAS antenna array is subject to field aliasing because of the spacing between the elementary antennas: the hexagonal field of view and its six neighbors are drawn in red, the Earth and its aliases are drawn in maroon, the sky and its aliases are drawn in blue, the ground incidence 60.6° is drawn in green, the black dot is the sub-satellite point with coordinates $(0, -\sin \epsilon)$.

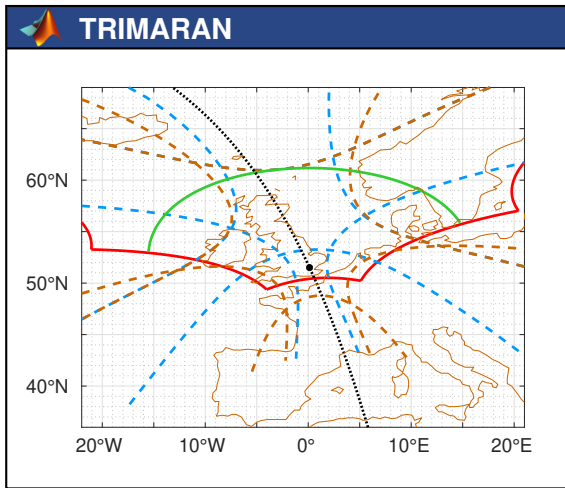


Figure 5: Hexagonal field of view of SMOS at ground level, as plotted by the function `geoplotFOV_hexa`. Referring back to Figure 4, here the sub-satellite point (black dot) is geo-localized over London and the ascending pass (black dotted curve) is that of a sun-synchronous circular orbit.

```
tilt,d,90,LonS,LatS,60.6);
```

When designing an aperture synthesis imaging radiometer, these functions are very useful for making the required trade-off between various figures of merit that may depend from several parameters like the elevation h , the geometry of the antenna array and the spacing d as well as the tilt angle ϵ . . . This is the case, for example, of the useful ground swath that is returned by the twinned functions `swathFOV_cart` and `swathFOV_hexa` which has, together with the orbital period T , a direct impact on the revisit time:

```
> swath=swathFOV_hexa(h,i,'Asc', ...
    tilt,d,90,LonS,LatS)
swath = 1.4330e+06
```

In that case of SMOS, 1433 Km with an orbital period of 100 min is fully compatible with a revisit time of 3 days at the equator.

Finally, aperture synthesis is performed at instrument level with the aid of the computer. As a consequence, sampling grids are required for discretizing integral equations. The two functions `grids_cart` and `grids_hexa` return the values taken by the directions cosines and by the spherical angles over sampling grids as well as many other quantities:

```
> N = 128;
> [~,~,X,Y,Sxy,~,Theta,Phi]= ...
    grids_hexa(h,tilt,d,90,N);
```

Θ and Φ are 1×2 cell arrays with the spherical angles θ and ϕ , respectively. X and Y are also 1×2 cell arrays with the components of ξ : $\xi_1 = \sin\theta \cos\phi$ and $\xi_2 = \sin\theta \sin\phi$, respectively. Sxy is the elementary area $d\xi$ of a pixel in the corresponding sampling

grid. For every 1×2 cell array, the first element $\{1\}$ is a $N \times N$ array limited to the field of view synthesized by the antenna array whereas the second one $\{2\}$ is a $2N \times 2N$ array with the corresponding quantity in the space $0 \leq \theta \leq \pi/2$ and $0 \leq \phi \leq 2\pi$ in front of the instrument. Among the other quantities returned by these two functions, very useful ones are the indices of the pixels from the grids X and Y that belong to the Earth or to the sky in the field of view, returned in 1×2 cell arrays `PXLearth` and `PXLsky`.

2.4 Antenna Patterns

Elementary antenna patterns are at the heart of antennas arrays. Although TRIMARAN is able to digest any measured pattern, the `AVP` function returns a voltage pattern that follows a $\cos^n \theta$ law (Anterrieu et al., 2003) with n related to the shape of the main beam:

```
> F{2}=AVP(Theta{2},Phi{2}-30,60,70);
> figure;plotAPP(X{2},Y{2},F{2},[-50 10]);
```

TRIMARAN has a family of functions `AVPestim*` and `APPestim*` to estimate parameters of voltage or power patterns like directivity D and equivalent solid angle Ω as defined by Equations (2–23) and (2–24) in (Balanis, 2005), Full-Width at Half-Maximum (FWHM). . . Hereafter are the lines to estimate these figures of merit for the power pattern of Figure 6:

```
> Omega=APPestimESA(F{2},[],X{2},Y{2},Sxy)
Omega = 12.5664
> D=APPestimDIR(F{2},[],X{2},Y{2},Sxy)
D = 10.0509
> FWHM=APPestimFWHM(F{2},X{2},Y{2})
```

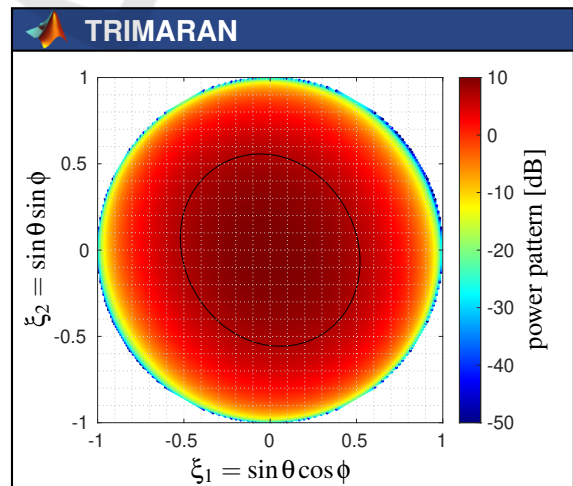


Figure 6: An example of a power pattern $|\mathcal{F}(\xi)|^2$, as returned by the function `AVP` and plotted by the function `plotAPP`. Black ellipse is the half-maximum power contour.

FWHM = 70.0000 60.0000 -60.0000

2.5 Instrument Modeling

According to the Van-Cittert Zernike theorem (van Cittert, 1934; Zernike, 1938) and referring to Figure7, the theoretical complex visibility V_{pq} for a pair of elementary antennas \mathcal{A}_p and \mathcal{A}_q in the far-field approximation is given by the relation:

$$V_{pq} = \iint_{\|\xi\| \leq 1} \frac{\mathcal{F}_p(\xi)}{\sqrt{\Omega_p}} \frac{\mathcal{F}_q^*(\xi)}{\sqrt{\Omega_q}} T(\xi) \tilde{r}_{pq} \left(-\frac{\mathbf{b}_{pq} \cdot \xi}{c} \right) \times e^{-2j\pi \frac{\mathbf{b}_{pq} \cdot \xi}{\lambda_o}} \frac{d\xi}{\sqrt{1 - \|\xi\|^2}}, \tag{1}$$

where \mathbf{b}_{pq} is the baseline vector between \mathcal{A}_p and \mathcal{A}_q , the components $\xi_1 = \sin \theta \cos \phi$ and $\xi_2 = \sin \theta \sin \phi$ of the angular position variable ξ are direction cosines in the reference frame of the array, θ and ϕ are the traditional spherical coordinates (the colatitude and the azimuth, respectively), $\mathcal{F}_p(\xi)$ and $\mathcal{F}_q(\xi)$ are the voltage patterns of the two elementary antennas with equivalent solid angles Ω_p and Ω_q , $T(\xi)$ is the brightness temperature distribution of the scene under observation, $\tilde{r}_{pq}(t)$ is the so-called fringe-washing function which accounts for spatial decorrelation effects for $t = -\mathbf{b}_{pq} \cdot \xi / c$ and $\lambda_o = c / f_o$ is the central wavelength of observation.

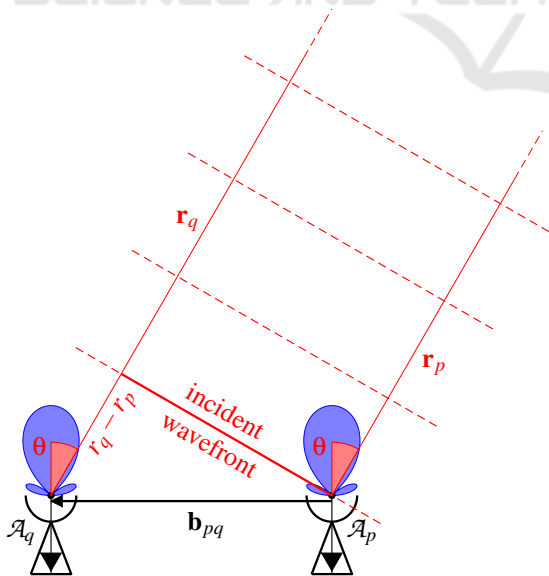


Figure 7: Two elementary antennas \mathcal{A}_p and \mathcal{A}_q pointing in the same direction, here the Nadir as illustrated by the main beam of the power patterns (in blue), \mathbf{r}_p and \mathbf{r}_q are location vectors with respect to the far-field source and the two antennas are separated by the baseline vector \mathbf{b}_{pq} .

The previous integral equation is implemented in the function `GT_sai`. Hereafter are the few lines to obtain the 4695 complex visibilities of MIRAS corresponding to an artificial scene that is set to a constant temperature 100 K over Earth and 0 K elsewhere:

```
> T=zeros(2*N,2*N); T(PXLearnth{2})=100;
> Vpq=GT_sai(Fo,Bo,F{2}./sqrt(Omega), ...
            P,Q,Ub,Vb,[], ...
            X{2},Y{2},Sxy,0,T);
> figure;plotVIS(Ub*Lo,Vb*Lo, ...
                vis2vis(P,Q,Vpq),'abs');
```

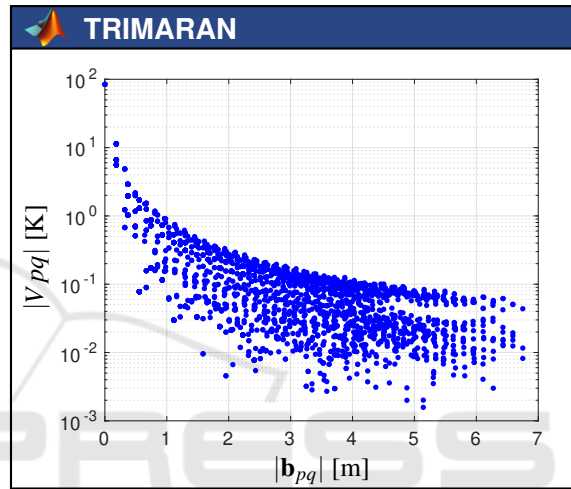


Figure 8: Magnitude of the complex visibilities V_{pq} of a flat scene T_b at a constant temperature 100 K, as plotted by the function `plotVIS`.

Referring back to the sampling grids introduced earlier in this section, after discretization of the integral found in (1) the relationship between the complex visibilities and the brightness temperature distribution of the scene under observation can be written in the algebraic form:

$$V = \mathbf{G}T \tag{2}$$

where \mathbf{G} is the linear modeling matrix of the imaging radiometer returned by the function `matG_sai`:

```
> G=matG_sai(Fo,Bo,F{1}./sqrt(Omega), ...
            P,Q,Ub,Vb,[],X{1},Y{1},Sxy);
```

The inverse problem which aims at inverting relation (2) is ill-posed as a consequence of the rank deficiency of \mathbf{G} which is illustrated by the distribution of its singular values, as shown in Figure 9 where two groups are well separated by a large gap.

```
> rank(G)
ans = 2791
> svG=svd(G);
> [T,idxT]=getThresholdSV(svG,Uf,Vf)
T = 8.8343e-04
```

```
idxT = 2791 2792
> figure;plotSV(svG,[1 idxT(1)]);
```

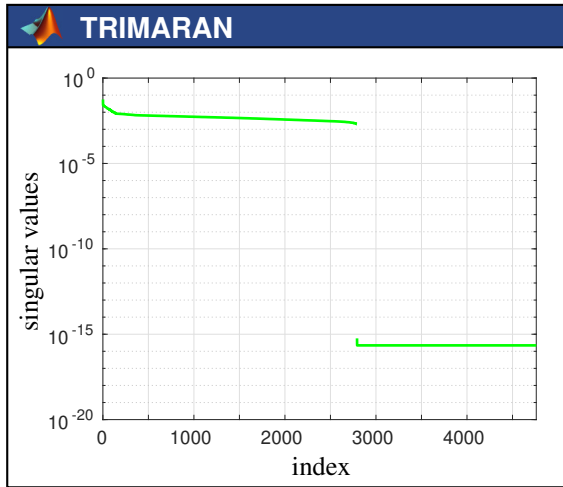


Figure 9: Distribution of the singular values of the modeling matrix \mathbf{G} , as plotted by the function `plotSV`.

As a consequence, the smallest ones have to be discarded prior the inversion to obtain a regularized version of \mathbf{G}^+ :

```
> Gp=pinv(G,T);
> Tr=reshape(Gp*Vpq,[N N]);
> figure;plotBTM(X{1},Y{1},Tr,[]);
> plotFOV_hexa(h,tilt,d,90,[]);
```

Shown on Figure 10 is the brightness temperature $T_r = \mathbf{G}^+V$ thus obtained. TRIMARAN offers alternative methods (Picard and Anterrieu, 2005) to this popular truncated singular value decomposition (Goodberlet, 2000) among which the regularizing approach implemented for SMOS (Anterrieu, 2004), the Tikhonov one (Tikhonov and Arsenin, 1977) and few total variation approaches (Chambolle, 2004).

The same kind of simulation can be performed but with the brightness temperature distribution of a point source, so that the Point-Spread Function (PSF) of the instrument can be estimated. This is exactly what is done very simply by the function `PointSpreadFunction` as shown on Figure 11.

```
> PSF=PointSpreadFunction(Uf,Vf,N);
> figure;plotBTM(X{1},Y{1},PSF,[]);
> axis([-1 1 -1 1]*0.1);
```

The function `ApodizationWindow` returns an apodization window that can be chosen among many and apply to any brightness temperature map with the aid of the function `apodizeBTM`. With regards to any PSF, wether it is apodized or not, the two functions `AngularResolution` and `GroundResolution` offer facilities to estimate the angular resolution at instru-

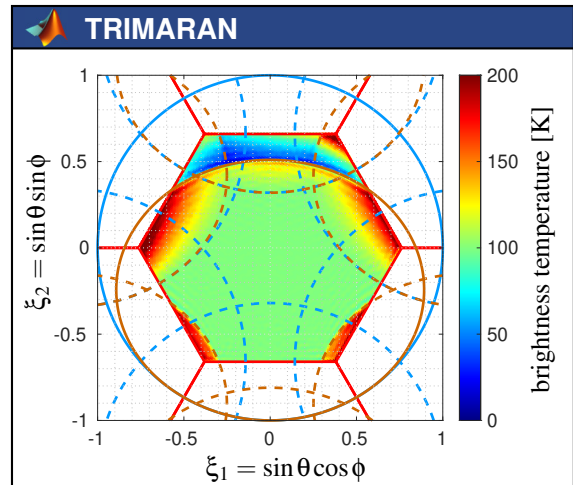


Figure 10: Retrieved brightness temperature map $T_r = \mathbf{G}^+V$, as plotted by the function `plotBTM`. Referring back to Figure 4, Earth aliases are clearly visible exactly where they are supposed to be. In the Earth alias-free part, the retrieved temperature is the expected one.

ment level and the spatial one at ground level, respectively.

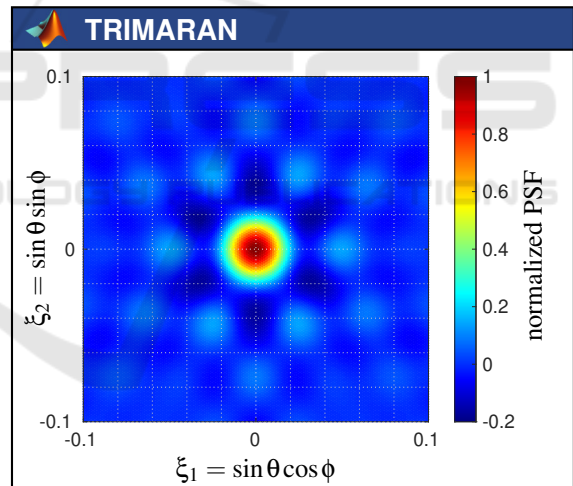


Figure 11: Normalized PSF of MIRAS antenna array, as plotted by the function `plotBTM` in the reduced domain $-0.1 \leq \xi_1 \leq 0.1$ and $-0.1 \leq \xi_2 \leq 0.1$.

Finally, additive synthesis with digital beam forming is available in TRIMARAN with the functions `GT_dbf` and `matG_dbf` which implement the integral relation between $T(\xi)$ and the antenna array temperature $\mathbb{T}(\xi')$ from a direction ξ' :

$$\mathbb{T}(\xi') = \iint_{\|\xi\| \leq 1} \frac{|\mathbb{F}_{\xi'}(\xi)|^2}{\Omega_{\xi'}} T(\xi) \frac{d\xi}{\sqrt{1 - \|\xi\|^2}}, \quad (3)$$

where

$$\mathbb{F}_{\xi'}(\xi) = \sum_{p=1}^M \mathcal{F}_p(\xi) e^{-2j\pi \frac{r_p}{\lambda} (\xi - \xi')} \quad (4)$$

is the voltage pattern of the antenna array when pointing in the direction ξ' and with equivalent solid angle $\Omega_{\xi'}$. The antenna array patterns $\mathbb{F}_{\xi'}(\xi)$ are calculated in the `ArrayAVP` function and their equivalent solid angle $\Omega_{\xi'}$ is returned by the function `AVPestimESA`. An example of $\mathbb{F}_{\xi'}(\xi)$ is shown on Figure 12. As expected, it is much narrower than the elementary pattern $\mathcal{F}(\xi)$ shown in Figure 6 and more directive as its directivity returned by `APPestimDIR` is about 42.5 dB (this is equal to that of $\mathcal{F}(\xi)$, which is about 10 dB, augmented by the number of elementary antennas (here $M = 69 \simeq 36.8$ dB) and reduced by the attenuation $\mathcal{F}(\xi')/\mathcal{F}(0) \simeq -4.3$ dB).

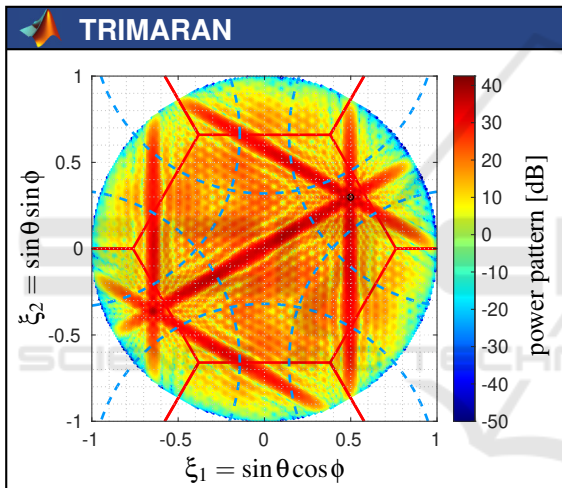


Figure 12: An example of antenna array power pattern $|\mathbb{F}_{\xi'}(\xi)|^2$ when pointing in the direction $\xi' = (0.5, 0.3)$, as returned by the function `ArrayAVP` and plotted by the function `plotAPP`. Here again, referring back to Figure 4, aliases are where they are supposed to be, as illustrated by the grating lobe in the direction $\xi = (-0.64, -0.36)$.

2.6 Radio Signals

It is sometimes necessary to work at the level of the signal kept by the elementary antennas (Anterrieu et al., 2017), particularly when the assumptions accompanying the Van-Cittert Zernike theorem are not satisfied. Although these calculations are time consuming ones, thanks to GPU usage in functions `RadioSignal` and `RadioSignalCal`, when such accelerators are found on the computer and when the Parallel Computing Toolbox (The MathWorks, b) is available, computational time can be reduced down to acceptable values, depending on the sampling fre-

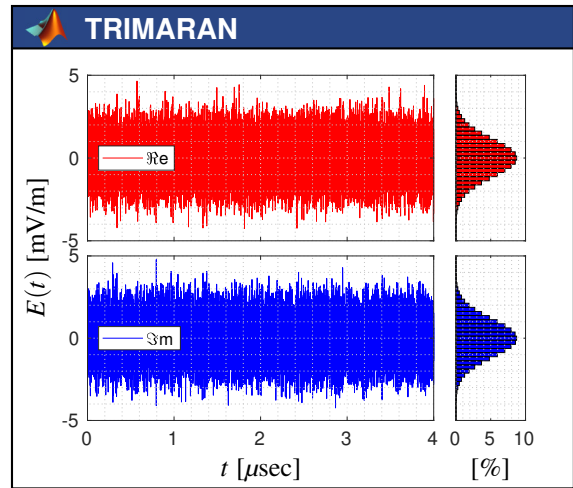


Figure 13: First samples of a (complex-valued) radio signal simulated by `RadioSignal` with $f_s = 8$ GHz, as plotted by the function `plotEMF`.

quency f_s and on the duration T_s of the signal to simulate. Shown on Figure 13 is an example of radio signal kept by an element of MIRAS. As shown on Figure 14 this signal is not just a white noise with a Gaussian Probability Density Function (PDF) in the time domain: its Power Spectral Density (PSD) in the frequency domain is that of a black body at the temperature of the scene (returned by the function `PlanckLaw`), as expected. Accounting for this coloration of the spectrum (obtained with a FIR filter returned by the function `FirPlanckLaw`) as well as for the propagation times between each pixel of the source and any antenna (evaluated by the function `FlyingTime`) to take into account the Doppler effect, explain the consequent calculation time for such sim-

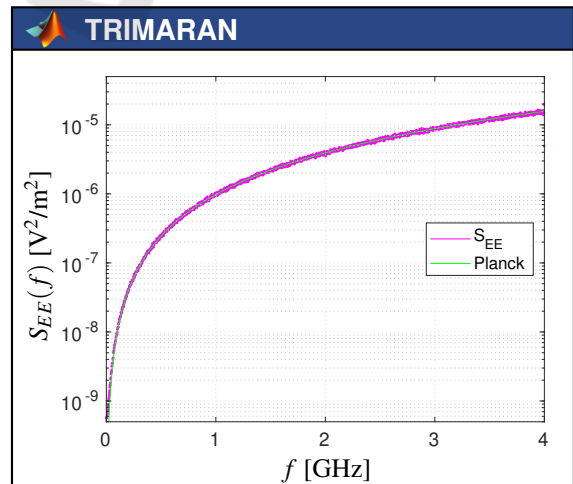


Figure 14: PSD of the radio signal shown on Figure 13, as computed by the function `PSDwelch` and plotted with Matlab's function `semilogy` in the range $0 \leq f \leq f_s/2$.

ulations. When filtering the signal of Figure 13 in the $B_o = 20$ MHz band centered on $f_o = 1413.5$ MHz (with an appropriate Raised-cosine filter calculated with the function `RcosFIR`) it turns out that the auto-correlation is about 84 K which is the value of the complex visibilities V_{pq} shown in Figure 8 for $|\mathbf{b}_{pq}| = 0$, as expected.

3 ILLUSTRATIVE EXAMPLES

TRIMARAN has been used from the very early studies of SMOS (for designing the antenna array of MIRAS as well as for evaluating its imaging performances) to the latest ones after launch, during commissioning (for checking radiometric sensitivity, angular resolution...) and since throughout the operational phase (for reducing floor error, detecting and localizing RFI sources...). The latest concrete usages of TRIMARAN are briefly presented to illustrate the capabilities of this toolbox when addressing various problems encountered in modern aperture synthesis.

3.1 Interferometry vs. Beam Forming

More recently, TRIMARAN has been used in a study (Anterrieu et al., 2022) to quantify the difference between two paradigms: on one hand synthetic aperture interferometry also known as multiplicative synthesis, and on the other hand digital beam forming also known as additive synthesis. Simulations have been conducted with MIRAS, the single payload of the SMOS mission. Three figures of merit have been targeted at image synthesis level: the floor error, the radiometric sensitivity and the angular resolution. No difference has been observed on the sensitivity nor on the resolution. On the contrary, the floor error (Duran et al., 2015) that is observed in the retrieved brightness temperature maps in the absence of any error or noise in the complex visibilities turns out to be at a higher level in the operational mode of MIRAS, i.e. synthetic aperture interferometry, than with digital beam forming if this paradigm has been chosen. This difference is illustrated on Figure 15 with simulations conducted with the brightness temperature distributions of a typical scene over the ocean (eq. [5] in (Zine et al., 2008)) in H and V polarizations. Oscillations and artifacts clearly appear in the brightness temperature maps retrieved with synthetic aperture interferometry, especially at low incidence angles, but not only, whereas they are almost absent, or at least strongly reduced, with digital beam forming. Quantitatively, the RMSE is reduced by about 0.4 K, which is not negligible with regards to

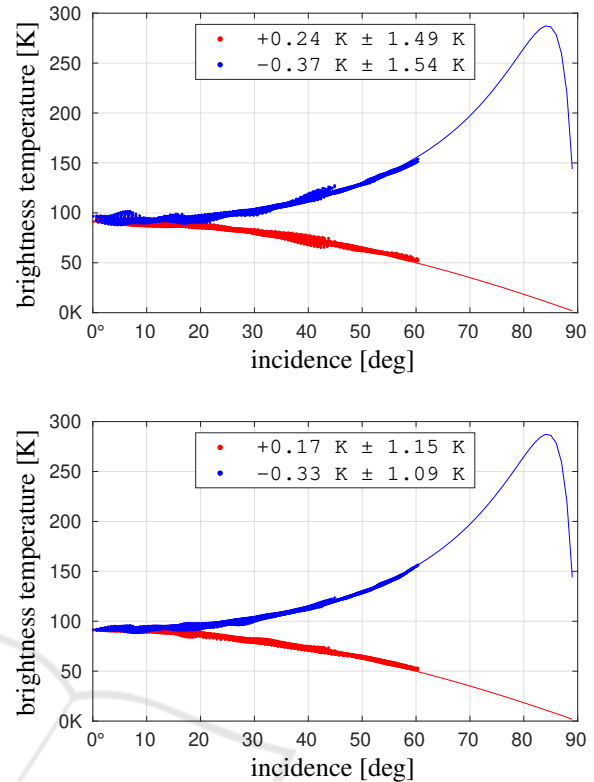


Figure 15: Variations of the retrieved temperatures in H (red dots) and V (blue dots) polarizations as well as those of the temperatures (lines) of the scene with the ground incidence angle when MIRAS is operating synthetic aperture interferometry (top) and if digital beam forming was the instrumental paradigm (bottom). The RMSE is about 1.51 K in H and 1.59 K in V for the first case, whereas it is about 1.16 K in H and 1.14 K in V for the second one.

a mission's target accuracy of 0.1 PSU with a sensitivity of the surface salinity which varies from 1 K down to 0.1 K per PSU (Font et al., 2004).

The origin of this difference has been found in the distribution of the singular values of the modeling operators of the two paradigms. As illustrated on Figure 16, whatever the approach, two groups of singular values separated by a well-determined gap are observed. In every case, the first group is composed of the 2791 largest singular values: the rank of the two matrices is equal to 2791, as expected. However, in the SMOS operational case (with 69 different antenna patterns), this gap is narrower than in the ideal case (with the same voltage pattern for each antenna). On the contrary, if MIRAS was operating digital beam forming, it would be less sensitive to the disparity between elementary patterns as this gap remains of the same order. This is why digital beam forming is the target paradigm for the FRESCH mission (Rodríguez-Fernández et al., 2024) that has been

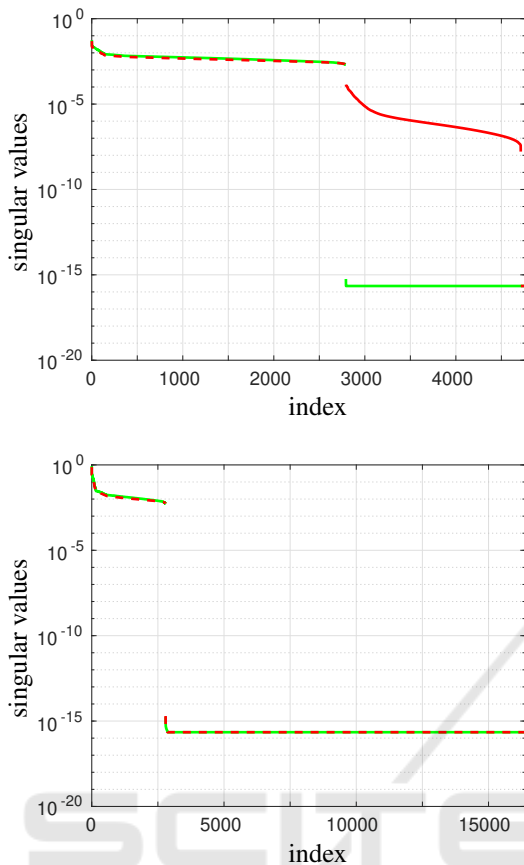


Figure 16: Distribution of the singular values of the modeling matrices of MIRAS when operating synthetic aperture interferometry (top) and if digital beam forming was the instrumental paradigm (bottom): in both cases, the elementary patterns are those measured on ground (red) or an ideal one (green).

proposed to ESA to continue MIRAS measurements whereas synthetic aperture interferometry of SMOS is only a backup principle.

3.2 Linear Algebra vs. Deep Learning

TRIMARAN has also been used in a recent study (Faucheron et al., 2024) to explore a deep learning based approach for inverting complex visibilities, an alternative to the algebraic methods used for decades in aperture synthesis. Brightness temperatures taken from SMOS L3 products (Al-Bitar et al., 2017) have been used to simulate a large dataset of brightness temperature maps T and complex visibilities V which has been split into three subsets according to:

- 60% of the dataset has been dedicated to the training subset, during which a Deep Neural Network (DNN) is exercised to the relation between V

and T ;

- 20% of the dataset has been used for the validation subset, during which the DNN learning is monitored on T/V pairs not used for the training;
- 20% have been devoted to the testing subset, which aims at comparing the performances of this data-driven approach to the algebraic inversion approach implemented in SMOS L1 ground segment processor, again with not previously used T/V pairs.

Shown on Figure 17 is an example taken from the testing subset of retrieved brightness temperature maps over Great Britain. The first difference to be noted is a larger reconstructed field of view without any aliasing in the deep learning based approach. This unexpected property is opening a new era for the design of future imaging radiometers with antenna arrays as the spacing between the elementary antennas which governs the field aliasing will no longer be a constrained driver of the imaging performances par-

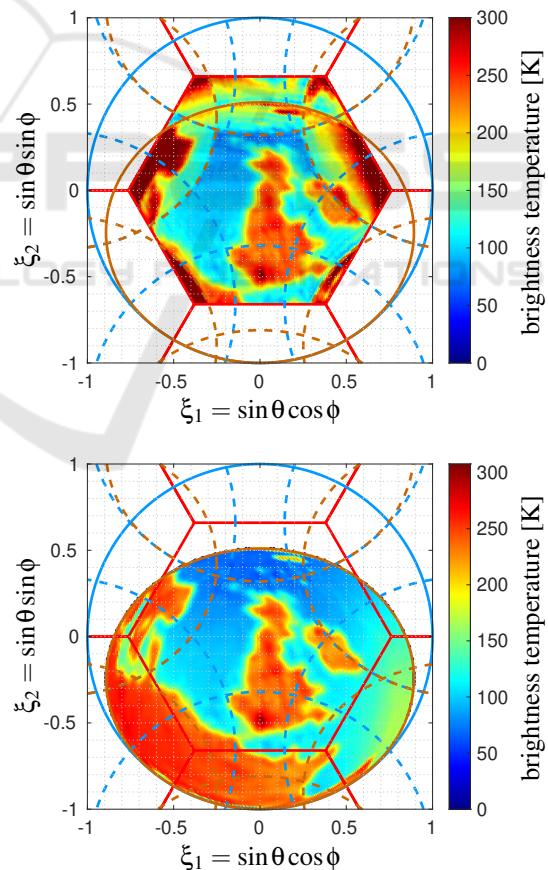


Figure 17: A representative example of brightness temperature maps retrieved from complex visibilities with SMOS operational algebraic inversion (top) and with a deep learning one (bottom). In both cases no apodization window has been used.

icipating to the trade-offs. On the contrary, the choice of this spacing can be left entirely to the elementary antennas designers with electromagnetism considerations for reducing coupling effects between elements.

Finally, the average RMSE over the entire testing subset in the Earth alias-free field of view is about 7.8 K with the operational algebraic inversion whereas it is only about 1 K with the deep learning one.

3.3 Near-Field vs. Far-Field

The latest and most recent published usage of TRIMARAN is a study devoted to the comparison between far-field and near-field conditions in synthetic aperture interferometry (Anterrieu et al., 2024). While there is no clear boundary between these regions, a common and acceptable criterion is that $2D^2/\lambda_o$ represents a safe limit between far-field and near-field, where D is the diameter of an elementary antenna and λ_o is the central operating wavelength. This criterion has been extended to antennas arrays where D is now the longest baseline between the elementary antennas (Selvan and Janaswamy, 2017). However, from the imaging point of view this criterion might not be sufficiently strict and should perhaps be revisited. This is exactly what has been observed in this study where the differences between far-field conditions shown in Figure 7 and near-field ones as illustrated by Figure 18 have been listed and taken into account to lead to the following modeling:

$$V_{pq} = \int \int_{\|\xi\| \leq 1} \frac{\mathcal{F}_p(\xi_p)}{\sqrt{\Omega_p}} \frac{\mathcal{F}_q^*(\xi_q)}{\sqrt{\Omega_q}} T(\xi) \frac{r^2(\xi)}{r_p(\xi)r_q(\xi)} \times e^{-2j\pi \frac{r_q(\xi) - r_p(\xi)}{\lambda_o}} \frac{d\xi}{\sqrt{1 - \|\xi\|^2}}, \quad (5)$$

where ξ_p and ξ_q are local direction cosines to account for the true vectors \mathbf{r}_p and \mathbf{r}_q in comparison with the direction ξ from the phase center of the array. This modeling is available in TRIMARAN with the functions `GT_sai_nf` and `matG_sai_nf`, with the aid of the function `FlyingTime` for calculating the real distances. Shown on Figure 19 are the singular values of the modeling operator of MIRAS in far-field conditions and in near-field ones when the elementary antennas are ideal ones with the same voltage pattern: the effect of the distance is similar to that of the diversity of the elementary patterns observed on Figure 16 with a reduction of the gap between the two groups of singular values.

As an illustration of the impact of the distance between the antenna array and a source, shown on Fig-

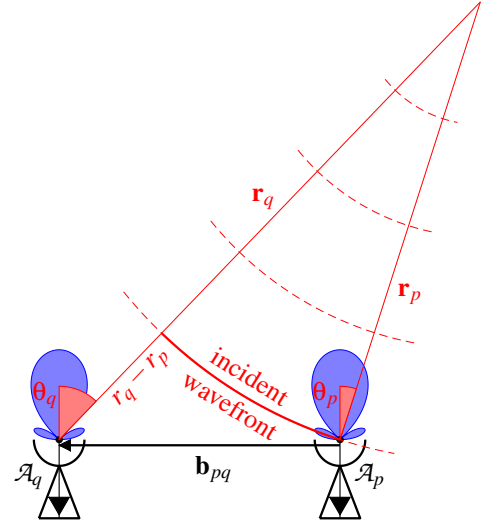


Figure 18: Two elementary antennas \mathcal{A}_p and \mathcal{A}_q pointing in the same direction, here the Nadir as illustrated by the main beam of the power patterns (in blue), \mathbf{r}_p and \mathbf{r}_q are location vectors with respect to the near-field source and the two antennas are separated by the baseline vector \mathbf{b}_{pq} . Contrary to far-field conditions of Figure 7 where incident waves are planes ones, here they are spherical.

ure 20 are the complex visibilities of a point source located in the direction $\xi = (0, 0)$ of MIRAS and at a distance from the phase center which is in the far-field region and closer in the near-field zone. Here again the difference is significant and one can imagine that the inversion has to be done with the appropriate operator, whatever the regularizing approach. Indeed, when inverting near-field visibilities with the inverse of a modeling operator in the far-field approximation the result might be surprising and unexpected. This is

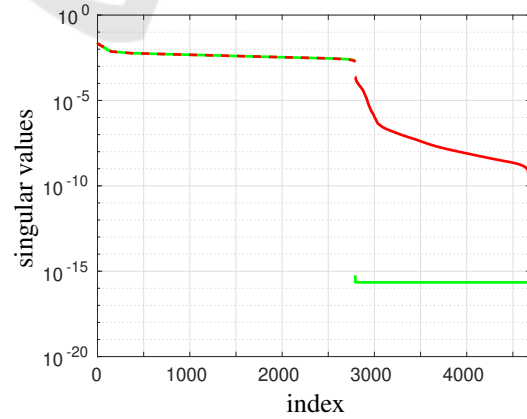


Figure 19: Distribution of the singular values of the modeling matrices of MIRAS when operating in the far-field region (green) and in the near-field zone (red): in both cases the same ideal voltage pattern has been used for every elementary antenna.

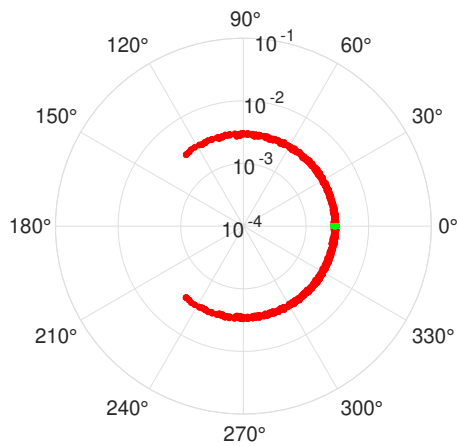


Figure 20: Complex visibilities of a point source located in the Nadir direction $\xi = (0, 0)$ of MIRAS and at a distance from the phase center which is in the far-field region (green) and closer in the near-field zone (red).

exactly what is shown on Figure 21 which has to be compared to Figure 11. Of course, when the appropriate near-field modeling operator is used, there is no difference between near-field and far-field impulse responses.

As already suggested in the literature, this study has proven that $2D^2/\lambda_o$ is not sufficiently strict for estimating a safe limit between far-field and near-field regions in aperture synthesis imaging applications. Indeed, it is always found to be among the lowest values of many figures of merit for this transition interval between these two regions. In the specific case of SMOS, a criterion around $10D^2/\lambda_o$ might be more appropriate to preserve the imaging performances of MIRAS. However, in the words of the authors of this study “*it would be very presumptuous to claim to change the definition of this criterion solely on the basis of a comparative study conducted with a single antenna array*”.

4 CONCLUSION

TRIMARAN, a Toolbox for Radiometric Imaging with Microwave ARrays of ANtennas, as been briefly described. It is a self-sufficient collection of about 200 Matlab functions that offer to users the opportunity to play numerically with multiplicative and additive synthesis, from the simulation of the radio signals kept by each elementary antenna to their combination to produce either complex visibilities (when operating interferometry) or antenna array temperatures (when beam forming is the paradigm) up to their processing with up-to-date regularized inversion methods to retrieve the brightness temperature distribution of the

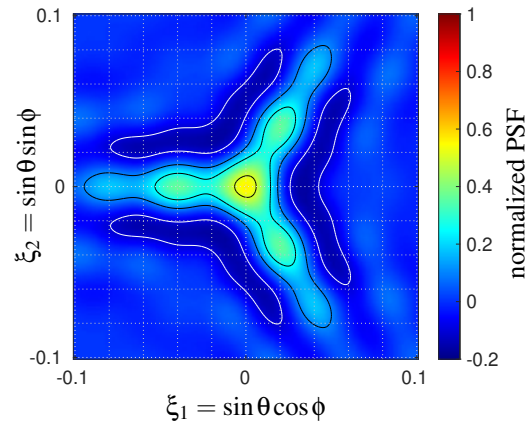


Figure 21: Normalized PSF of MIRAS antenna array obtained when inverting near-field visibilities (the red ones of Figure 20) with the inverse of the modeling operator of MIRAS in the far-field approximation.

scene under observation.

In addition to this overview, some concrete usages made by researchers, engineers or students have been shown to illustrate the capabilities of TRIMARAN for designing aperture synthesis imaging radiometers and for quantifying instrument performances as well as for discovering and for learning many aspects of microwave remote sensing by aperture synthesis with realism. In every case, this is done with very few lines of code to write, thanks to high-level functions that can digest simulated data as well as real ones from an actual instrument, in ground based as well as in airborne or spaceborne situations.

ACKNOWLEDGEMENTS

The author is very grateful to all those, engineers, researchers, teachers and students, who have used, criticized and therefore improved TRIMARAN.

REFERENCES

- Al-Bitar, A., Mialon, A., Kerr, Y., Cabot, F., Richaume, P., Jacquette, E., Quesney, A., Mahmoodi, A., Tarot, S., Parrens, M., Al-Yaari, A., Pellarin, T., Rodriguez-Fernandez, N., and Wigneron, J.-P. (2017). The global smos level 3 daily soil moisture and brightness temperature maps. *Earth System Science Data*, 9(1):293–315.
- Anterrieu, E. (2004). A resolving matrix approach for synthetic aperture imaging radiometers. *IEEE Transactions on Geoscience and Remote Sensing*, 42(8):1649–1656.
- Anterrieu, E., Cabot, F., Khazâal, A., and Kerr, Y. (2017). On the simulation of complex visibilities in imaging

- radiometry by aperture synthesis. *IEEE Journal of Selected Topics in Applied Earth Observations and Remote Sensing*, 10(11):4666–4676.
- Anterrieu, E., Gratton, S., and Picard, B. (2003). Self characterization of modelling parameters for synthetic aperture imaging radiometers. In *Proc. of IEEE International Geoscience and Remote Sensing Symposium (IGARSS)*, volume 5, pages 3052–3054.
- Anterrieu, E., Lafuma, P., and Jeannin, N. (2022). An algebraic comparison of synthetic aperture interferometry and digital beam forming in imaging radiometry. *MDPI Remote Sensing*, 14(9):2285.
- Anterrieu, E., Yu, L., and Jeannin, N. (2024). A comprehensive comparison of far-field and near-field imaging radiometry in synthetic aperture interferometry. *MDPI Remote Sensing*, 16(19):3584.
- Balanis, C. (2005). *Antenna theory: analysis and design*. John Wiley & Sons, Hoboken (NJ), USA, 3rd edition.
- Barré, H., Duesmann, B., and Kerr, Y. (2008). Smos: the mission and the system. *IEEE Transactions on Geoscience and Remote Sensing*, 46(3):587–593.
- Brouw, W. (1975). *Aperture Synthesis*. Elsevier, Amsterdam, The Netherlands, 1st edition.
- Chambolle, A. (2004). An algorithm for total variation minimization and applications. *Journal of Mathematical Imaging and Vision*, 20(1):89–97.
- Chang, K.-T. (2016). *Introduction to Geographic Information Systems*. McGraw-Hill, New-York (NY), USA, 9th edition.
- Christiansen, W. and Högbom, J. (1987). *Radiotelescopes*. Cambridge University Press, Cambridge, UK, 2nd edition.
- Cohen, M. (1973). Introduction to very-long baseline interferometry. *Proceedings of the IEEE*, 61(9):1192–1197.
- Duran, I., Lin, W., Corbella, I., Torres, F., Duffo, N., and Martin-Neira, M. (2015). Smos floor error impact and mitigation on ocean imaging. In *Proc. of IEEE International Geoscience and Remote Sensing Symposium (IGARSS)*, pages 1437–1440.
- Faucheron, R., Anterrieu, E., Yu, L., Khazâal, A., and Rodriguez-Fernandez, N. (2024). Deep learning based approach in imaging radiometry by aperture synthesis: an alias-free method. *IEEE Journal of Selected Topics in Applied Earth Observations and Remote Sensing*, 17(3):6693–6711.
- Font, J., Lagerloef, G., Vine, D. L., Camps, A., and Zanifé, O.-Z. (2004). The determination of surface salinity with the european smos space mission. *IEEE Transactions on Geoscience and Remote Sensing*, 42(10):2196–2205.
- Goodberlet, M. (2000). Improved image reconstruction techniques for synthetic aperture radiometers. *IEEE Transactions on Geoscience and Remote Sensing*, 38(3):1362–1366.
- The MathWorks. Matlab: The language of technical computing [online]. Available: www.mathworks.com/help/matlab/.
- The MathWorks. Parallel computing toolbox: Perform parallel computations on multicore computers, gpus, and computer clusters [online]. Available: www.mathworks.com/help/parallel-computing/.
- McMullan, K., Brown, M., Martin-Neira, M., Rits, W., Ekholm, S., and Lemanczyk, J. (2008). Smos: the payload. *IEEE Transactions on Geoscience and Remote Sensing*, 46(3):594–605.
- Napier, P., Bagri, D., Clark, B., Rogers, A., Romney, J., Thompson, A., and Walker, R. (1994). The very long baseline array. *Proceedings of the IEEE*, 82(5):658–672.
- Picard, B. and Anterrieu, E. (2005). Comparison of regularized inversion methods in synthetic aperture imaging radiometry. *IEEE Transactions on Geoscience and Remote Sensing*, 43(2):218–224.
- Rodriguez-Fernandez, N., Rixen, T., Boutin, J., Brandt, P., Corbari, C., Escorihuela, M.-J., Herrmann, M., Iovino, D., Landschutzer, P., Merkouriadi, I., Roy, A., Scholze, M., Kerr, Y., Anterrieu, E., Yu, L., Lamy, A., Gonzalez, P., Scala, F., Colombo, C., Gaias, G., Gutierrez, A., Lopes, G., Mège, A., Kallel, A., and Carayon, B. (2024). The fine resolution explorer for salinity, carbon and hydrology (fresch): a satellite mission to study ocean-land-ice interfaces. In *Proc. of IEEE International Geoscience and Remote Sensing Symposium (IGARSS)*, pages 6705–6708.
- Selvan, K. and Janaswamy, R. (2017). Fraunhofer and fresnel distances: unified derivation for aperture antennas. *IEEE Antennas and Propagation Magazine*, 59(4):12–15.
- Thompson, A., Clark, B., Wade, C., and Napier, P. (1980). The very large array. *Astrophysical Journal Supplement Series*, 44:151–157.
- Tikhonov, A. and Arsenin, V. (1977). *Solution of ill-posed problems*. Winston & Sons, Washington (DC), USA, 1st edition.
- van Cittert, P. (1934). Die wahrscheinliche schwingungsverteilung in einer von einer lichtquelle direkt oder mittels einer linse beleuchteten ebene. *Physica*, 1(1):201–210.
- Vine, D. L., Griffis, A., Swift, C., and Jackson, T. (1994). Estar: a synthetic aperture microwave radiometer for remote sensing applications. *Proceedings of the IEEE*, 82(12):1787–1801.
- Zernike, F. (1938). The concept of degree of coherence and its application to optical problems. *Physica*, 5(8):785–795.
- Zine, S., Boutin, J., Font, J., Reul, N., Waldteufel, P., Gabarró, C., Tenerelli, J., Petitcolin, F., Vergely, J.-L., Talone, M., and Delwart, S. (2008). Overview of the smos sea surface salinity prototype processor. *IEEE Transactions on Geoscience and Remote Sensing*, 46(3):621–645.